All-atomic and coarse-grained molecular dynamics investigation of deformation in semi-crystalline lamellar polyethylene

All-atomic and coarse-grained molecular dynamics investigation of deformation in semi-crystalline lamellar polyethylene

Pär A. T. Olsson[a,b,*], Pieter J. in 't Veld[c], Eskil Andreasson[d,e], Erik Bergvall[d],
Elin Persson Jutemar[d], Viktor Petersson[d], Gregory C. Rutledge[f], Martin Kroon[g]

[a]*Materials Science and Applied Mathematics, Malmö University, SE-20506 Malmö, Sweden*
[b]*Division of Mechanics, Lund University, Box 118, SE-22100 Lund, Sweden*
[c]*Polymer Physics, BASF SE, 38 Carl-Bosch Street, Ludwigshafen D-67056, Germany*
[d]*Tetra Pak, Ruben Rausings gata, SE-22186 Lund, Sweden*
[e]*Department of Mechanical Engineering, Blekinge Institute of Technology, SE-37179, Karlskrona, Sweden*
[f]*Department of Chemical Engineering, Massachusetts Institute of Technology, Cambridge, MA-02139, United States*
[g]*Department of Mechanical Engineering, Linneaus University, SE-35106 Växjö, Sweden*

Abstract

In the present work we have performed classical molecular dynamics modelling to investigate the effects of different types of force-fields on the stress-strain and yielding behaviours in semi-crystalline lamellar stacked linear polyethylene. To this end, specifically the all-atomic optimized potential for liquid simulations (OPLS-AA) and the coarse-grained united-atom (UA) force-fields are used to simulate the yielding and tensile behaviour for the lamellar separation mode. Despite that the considered samples and their topologies are identical for both approaches, the results show that they predict widely different stress-strain and yielding behaviours. For all UA simulations we obtain oscillating stress-strain curves accompanied by repetitive chain transport to the amorphous region, along with substantial chain slip and crystal reorientation. For the OPLS-AA modelling primarily cavitation formation is observed, with small amounts of chain slip to reorient the crystal such that the chains align in the tensile direction. This force-field dependence is rooted in the lack of explicit H-H and C-H repulsion in the UA approach, which gives rise to underestimated ideal critical resolved shear stress. The computed critical resolved shear stress for the OPLS-AA approach is in good agreement with density functional theory calculations and the yielding mechanisms resemble those of the lamellar separation mode. The disparate energy and shear stress barriers for chain slip of the different models can be interpreted as differently predicted intrinsic activation rates for the mechanism, which ultimately are responsible for the observed diverse responses of the two modelling approaches.

Keywords: Semi-crystalline polyethylene, Plasticity, Molecular dynamics

1. Introduction

For high density linear polyethylene (PE), the microstructure consists primarily of semi-crystalline spherulites with crystalline lamellae and amorphous layers of varying thickness sequentially arranged in an alternating manner [1, 2]. In the stress free state, the lamellae crystals are commonly lozenge shaped with the chains arranged according to an orthorhombic unit cell. The polymer chains are folded back and forth in the crystal multiple times, such that they are primarily aligned parallel to the orthorhombic c-axis and that the lozenge surface normal direction corresponds to the [001]-direction [1–5]. Thus, the strong covalent bonding dominates in the c-direction, whereas weak van der Waals (vdW) interaction is the predominant bonding type in the transverse directions. The polymer is held together by entangled segments and bridge-molecules that extend from one crystal stack through the amorphous part to the neighboring crystal and possibly even further. The density of the polymer and the molecular structure depend on the manufacturing technique and process timings. The thickness of the crystalline lamellae typically lies in the range 3-25 nm, whereas the lateral dimensions can reach up to 50 μm [1–5].

Yielding of semi-crystalline polymers is characterized by the interplay of complex and widely different plastic deformation mechanisms in the crystalline and amorphous parts of the polymer. Typically, the amorphous parts behave in a ductile manner and can accommodate substantial amounts of strain before rupture, whereas the crystalline parts are less ductile with the plastic deformations being constrained by preferential crystallographic orientations [2–9]. Specifically, the crystalline parts of PE yield mainly through three mechanisms: (i) slip [3–5, 10–19], (ii) twinning [3, 18–22] and (iii) martensitic transformation [3, 19, 21–24], of which the former is most frequently observed. The most important slip modes involve shearing parallel to the [001]-direction, which is commonly referred to as chain slip. Such deformation proceeds mainly by the activation of the (100)[001] or (010)[001]-slip systems, of which the former slip system has been found to exhibit the least resistance [4, 10–14]. Hence, depending on the degree of crystallinity of the material, widely different mechanical properties can be obtained, which complicates the general prediction of the me-

chanical response.

To gain insight into the complex behaviour of semi-crystalline polymers, atomistic modelling is a useful numerical modelling tool that has been widely used in the literature [25–44]. Most of these works have been based on simplified and coarse-grained interaction models, such as the united atom (UA) interaction model. In the UA approach, the hydrogen and carbon backbone atoms are lumped together to form united CH_x particles (or super atoms), whose interparticle interaction is described by a coarse-grained potential [45]. Such force-fields are effective interactions that incorporate the effects of the neglected degrees of freedom in a mean-field manner. Using such simplified interaction models is very beneficial from a numerical standpoint mainly for three reasons: (i) the number of degrees of freedom are reduced by approximately a factor of three, (ii) the explicit interaction models are simpler and (iii) the utilized timestep increment can be much larger than for all-atomic (or explicit) approaches.

Among the aforementioned works, Rutledge and co-workers recently published a series of papers dealing with molecular dynamics (MD) modelling of yielding of PE [25–30] and other semi-crystalline polymers, such as polyurethane [31, 32] and polyether [33]. These investigations have revealed that there is a strain rate dependence that dictates the observed stress-strain behaviour and yielding mechanisms [25–28]. At high strain rate, cavitation in the amorphous domains is dominating, whereas for lower strain rates repeated melting events accompanied by transport of chains from the crystalline to the amorphous domain occur, which give rise to a violently oscillating stress-strain behaviour [25, 26]. It was further reported that cavitation was favoured when the crystal lamellae were thicker, which concurs with experimental results [46–48]. In addition to these results, it has been indicated that plastic fine slip occurs at relatively early stages of deformation in the crystalline regions, which manifests in crystal reorientation such that initially tilted chains align in the tensile direction [25, 26]. This is followed by additional chain slip that causes the initially straight crystalline-amorphous interface to become wavy [26]. These results partially agree with the results from all-atomic modelling [39], where cavitation formation in the amorphous region was found to be dominant. However, in contrast to the UA modelling, no reports of early onset of chain slip in the crystal regions were made.

The seemingly disparate yielding behaviours of the crystalline regions for the UA and all-atomic models motivated a comparative benchmarking study [14], in which the generalized stacking fault energy landscapes (or γ-surfaces [49]) for UA and all-atomic models were compared with results from *ab initio* density functional theory (DFT) modelling. The results showed that the activation energy barriers (or unstable stacking fault energy) associated with chain slip were much underestimated by the UA approach, whereas the all-atomic approach reproduced reasonably accurate data. The explanation behind the ability of the all-atomic approach to predict the γ-surface lies in the explicit H-H and C-H repulsion, of which especially the former is important to describe the generalized stacking fault energy. Thus, because the UA approach relies on coarse-grained particle dynamics wherein the explicit H-H repulsion is absent, underestimated activation energies for slip are likely unavoidable [14]. This insight raises the question of whether the UA approach is appropriate to model irreversible slip in the crystalline domains of PE?

To investigate this matter, in the present work we have performed a comparative MD study of the response of semi-crystalline PE by using an all-atomic and a UA interatomic potential. To this end we have modelled the behaviour of semi-crystalline PE subjected to uniaxial tensile loading in accordance with the postulated lamellar separation mode [50]. We have studied the deformation mechanisms and the stress-strain response, with special emphasis given to elucidate the potential crystal chain reorientation and slip deformation. This aims to give clarity to whether the shortcoming of low unstable stacking fault energy of UA force-fields has any substantial impact on the observed chain slip mechanisms, or if an all-atomic force-field is beneficial to predict the yielding behaviour?

The remainder of the paper is organized as follows. In Section 2 we introduce the simulation setups and provide computational details. Results are presented and discussed in Sections 3 and 4, respectively, while Section 5 contains our summary and conclusions.

2. Simulation setup and methodology

2.1. Interatomic potentials

For the MD modelling we use the LAMMPS software [51] and for the interatomic interaction, we adopt two existing strategies: the all-atomic optimized potential for liquid simulations (OPLS-AA) and UA approaches. The parameters for the OPLS-AA field emanate from [52–54] and the UA-potential parameters originate from Paul *et al.* [55], but were subsequently modified by Bolton *et al.* [56] and by in 't Veld and Rutledge [57]. The potential parameters were originally optimized to reproduce experimental conformations and thermodynamic properties of liquid and gas phase polymers [53, 55]. Such fitting databases mainly comprise equilibrium properties and therefore their predictive capabilities may be limited in non-equilibrium MD applications, which in part merits the present investigation.

For clarity we discuss the two force-fields here and the different contributions to the potential energy. For the covalent bonds, the bond stretch, E_{bond}, and angle bendings, E_{angle}, are represented by harmonic potentials, i.e.

$$E_{bond} = \frac{1}{2}K_b(r - r_0)^2 \tag{1}$$

and

$$E_{angle} = \frac{1}{2}K_\theta(\theta - \theta_0)^2 \tag{2}$$

while the dihedral chain deformations are governed by a cosine series potential

$$E_{dihedral} = \frac{1}{2}\sum_{n=1}^{3} K_n(1 - (-1)^n \cos n\phi) \tag{3}$$

2

Table 1: Parameters of the utilized empirical potentials. K_θ, K_n and ϵ are given in kcal/mol, K_b is given in kcal/(mol·Å²) and r_0 and σ are given in Å.

OPLS-AA				
C-C	K_b =536	r_0 = 1.529	ϵ =0.066	σ = 3.50
C-H	K_b =680	r_0 = 1.090	ϵ =0.045	σ = 2.96
H-H			ϵ =0.030	σ = 2.50
C-C-C	K_θ =118	θ_0 = 112.7°		
C-C-H	K_θ =75.0	θ_0 = 110.7°		
H-C-H	K_θ =66.0	θ_0 = 107.8°		
C-C-C-C	K_1 =1.74	K_2 =-0.157	K_3 =0.279	
C-C-C-H	K_1 =0.0	K_2 =0.0	K_3 =0.366	
H-C-C-H	K_1 =0.0	K_2 =0.0	K_3 =0.318	
UA				
CH_2-CH_2	K_b =634	r_0 = 1.530	ϵ =0.093	σ = 4.009
CH_2-CH_3	K_b =634	r_0 = 1.530	ϵ =0.145	σ = 4.009
CH_3-CH_3	K_b =634	r_0 = 1.530	ϵ =0.226	σ = 4.009
CH_x-CH_x-CH_x	K_θ =120	θ_0 = 110°		
CH_x-CH_x-CH_x-CH_x	K_1 =1.6	K_2 =-0.867	K_3 =3.24	

The non-bonded interaction consists of vdW-interaction and close-ranged repulsion described by the Lennard-Jones (L-J) 12-6 potential

$$E_{vdW} = 4\epsilon\left[\left(\frac{\sigma}{r}\right)^{12} - \left(\frac{\sigma}{r}\right)^{6}\right] \quad (4)$$

For the adopted potentials, the L-J contributions are limited by a cutoff at 12 Å for OPLS-AA and 10 Å for UA and we utilize long-range tail corrections for the energy and stress computations. The explicit parameters for the herein utilized potentials can be seen in Table 1.

Conventionally, for the OPLS-AA potential there are partial charges assigned to the C and H atoms that give rise to Coulombic interaction, which is absent in the UA approach because of the neutral charging of the lumped CH_x-particles. However, since the partial charges are relatively small (+0.06 for H, while that of C is determined by charge neutrality of the CH_x-groups), we neglect them in the present work and assume that all atoms are neutral. The impact of this simplified view on the results has been evaluated for chain slip in crystalline PE in connection with the preparation of [14], for which neglect of the Coulombic interaction emanating from the partial charges was found to reduce the unstable stacking fault energy of the (100)[001]-slip system from 9.1 to 8.7 mJ/m². Thus, the potential simplification leads to a reduction of the unstable stacking fault energy that is less than 5%, which we consider to be an acceptable approximation. The numerical benefit of not having to employ reciprocal k-space algorithms to account for Coulombic interaction was found to be substantial. Thus, the reduction in numerical cost greatly outweighs the loss in accuracy, which is why we assume charge neutrality for all H- and C-atoms in OPLS-AA framework.

2.2. Semi-crystalline sample generation

To generate the semi-crystalline samples we utilized the interphase Monte Carlo (IMC) approach as outlined by Rutledge and co-workers (see for instance [26–28]) and implemented in the Enhanced Monte Carlo open source software package [57]. Through this approach we generated periodic microstructures consisting of alternating crystalline and amorphous domains. The method, which is well-documented in [26–28], can be briefly summarized as a two-step procedure that consists of (i) initialization and (ii) site and chain connectivity altering Monte Carlo (MC) modelling. The first step aims to generate an initially fully crystalline sample in which chains are randomly cut and atoms removed to create a sample with the desired number of chain ends and density in the domain to become amorphous. In the following step, MC moves are employed to the atoms and chains in the amorphous domain to displace sites and alter the chain connectivity to create new loops, tails and bridges. The crystalline parts of the generated samples remain ideal, i.e. they are defect-free such that no dislocations or twins are present. Such defects are known to mitigate slip processes and reduce the critical shear stress substantially. Thus, the considered models are idealizations of a real semi-crystalline PE material and the anticipated resistance to crystal yielding is expected to be higher than experimentally observed.

The IMC simulations were performed using a UA representation with the particles interacting through the force-field parameters in Table 1. The considered MC moves applied to the amorphous region are of five different types that comprise single-site displacement, end-rotation, re-bridging, reptation and end-bridging. These moves were performed with the respective relative frequencies of 51%, 14%, 14%, 7% and 14%. To generate a truly random amorphous region a high MC trial acceptance rate is needed. Thus, we performed the MC modelling at an initially high temperature (10 000 K) and then gradually reduced it to 350 K. This gradual cooling was performed in 20 equally sized temperature reductions with each consisting of 8 000 MC cycles, which was sufficient to obtain realistic amorphous regions.

We post-processed the generated UA samples to create all-atomic configurations by introducing hydrogen atoms associated with each site, i.e. three hydrogen atoms bound to the car-

bon atoms at the chain ends and two associated with the other carbon atoms. The samples were subsequently imported into LAMMPS and equilibrated through MD simulations in the NPT ensemble at $T = 350$ K and $P = 1$ atm for 400 000 timesteps of 1 fs, by using the OPLS-AA force-field parameters from Table 1 as interaction model. The latter step was performed to obtain the equilibrium simulation cell and atomic configuration, as well as ensuring that the added H-atoms are sufficiently separated to avoid instabilities emanating from small interatomic separations. By using this post-processing strategy, for each sample we have generated an all-atomic and a UA representation of the semi-crystalline specimen with identical topologies. Since those samples are identical (except for the missing explicit H atoms in the UA samples), this enables us to perform a direct comparison of the mechanical response and yielding deformations between the two modelling approaches.

By using the outlined IMC approach, two sets of samples were created to investigate the impact of initial chain tilting relative to the tensile direction on the yielding. The first corresponds to the chains being aligned with the tensile direction, such that the interface between the crystalline and amorphous domain corresponds to the {001}-crystal plane whose normal direction is [001], see Figure 1(a) and (b). Because the Schmid factor is zero for chain slip of this orientation, we also consider systems with the chains tilted such that the interface plane corresponds to {201}, see Figure 1(c) and (d). This gives rise to an initial chain tilt of about 34° relative to the tensile direction.

The chosen sample sizes were $7 \times 11 \times 60$ orthorhombic unit cells ($a \times b \times c$) with the size of the amorphous domain corresponding to $7 \times 11 \times 30$. This yields a crystallinity of about 50%. The lattice parameters used for the IMC modelling concur with those found in [14] for the OPLS-AA approach, i.e. $a = 7.284$ Å, $b = 4.908$ Å, and $c = 2.541$ Å. To vary the chain connectivity of the samples, we utilized different numbers of chain cuts such that the number of free ends in the amorphous domain could be varied. Thus, either 60 or 154 free ends were created, i.e. 30 or 77 chains were cut, respectively, during the initial stage of the IMC modelling. In addition, to reduce the mass density of the amorphous region to about 0.8 g/cm^3 we randomly removed 1 386 carbon backbone sites at the created chain ends.

It should be noted that the primary objective of this work is not to provide an exhaustive study on how the topology affects the mechanical properties - it is rather to highlight and explain differences in the results for the two potentials. Thus, we limit the study to only consider the two sets of semi-crystalline samples.

Figure 1: Semi-crystalline samples with [001] stack normal direction with (a) two and (b) no bridges, respectively. Dito with [201] stack normal direction with (c) two and (d) no bridges, respectively. The springgreen sites indicate segments in the crystalline domain. The red, green and blue sites indicate bridge, loop and tail segments in the amorphous domain (the hydrogen atoms have been filtered out). The arrows schematically indicate the direction onto which the strain is applied. Periodic boundary conditions are applied in all directions. The figures are generated using the OVITO software [58]. (For interpretation of the references to colour in this figure, the reader is referred to the web version of this article.)

2.3. Topological characterization

To characterize semi-crystalline sample topology we use the algorithm outlined in [27], which enables us to distinguish four types of segments: crystal stems and amorphous tails, bridges and loops. Briefly summarized, this algorithm relies on computing the vectors $\mathbf{r}_{i-1}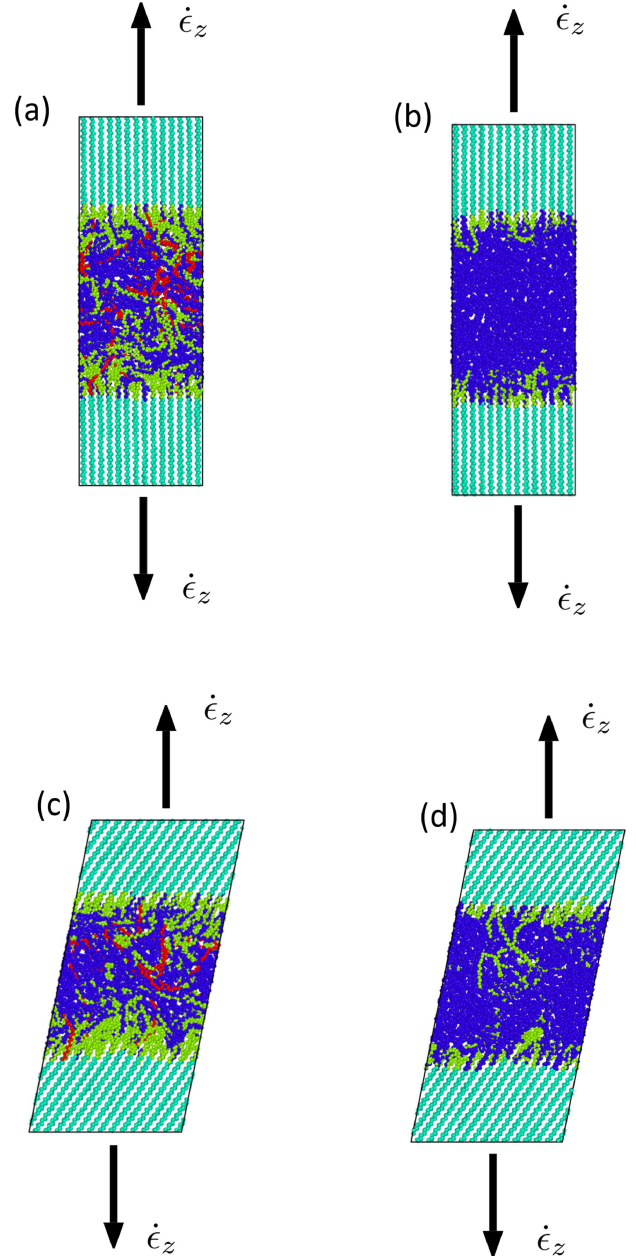$ and $\mathbf{r}_{i+1}$ from each site, i, to the nearest neighbouring sites of the same chain to identify the spatial orientation. Then we compute Herman's orientation parameter, $P_{2,i} = (3\langle \cos^2 \theta_{ij} \rangle - 1)/2$ for each site i. Here θ_{ij} represents the angle between the vectors $\mathbf{r}_{i+1} - \mathbf{r}_{i-1}$ and $\mathbf{r}_{j+1} - \mathbf{r}_{j-1}$, where j represents all sites located within the interaction range of the L-J potential.

Table 2: Topology evaluation of the samples generated and studied.

Sample	Crystal sites	Amorphous sites	No. bridges	bridge sites [%]	Tail sites [%]	Loop sites [%]	Cryst. plane
1	9979	7115	2	10.4	53.6	36.0	{001}
2	9901	7193	2	12.3	56.6	31.1	{001}
3	9936	7158	2	11.8	55.8	32.4	{001}
4	9957	7137	2	7.2	63.5	29.3	{001}
5	9895	7199	2	10.7	55.6	33.7	{001}
6	9979	7115	0	0	83.6	16.4	{001}
7	10012	7082	1	1.7	82.4	15.9	{001}
8	10022	7072	1	3.0	84.6	12.4	{001}
9	9944	7150	0	0	88.2	11.8	{001}
10	9965	7129	0	0	89.4	10.6	{001}
11	10169	6925	2	5.2	57.7	37.1	{201}
12	10172	6922	2	13.0	56.9	30.2	{201}
13	10088	7006	2	8.8	52.3	39.0	{201}
14	10135	6959	2	13.5	50.9	35.6	{201}
15	10168	6926	2	5.7	45.9	48.4	{201}
16	10220	6874	0	0	84.6	15.4	{201}
17	10289	6805	0	0	85.3	14.7	{201}
18	10252	6842	1	2.5	79.3	18.2	{201}
19	10267	6827	1	2.0	83.4	14.6	{201}
20	10158	6936	0	0	80.6	19.4	{201}

Any sites with $P_{2,i}$ larger than a threshold value (0.4 for UA and 0.55 for OPLS-AA) are considered to be crystalline and the remaining are designated amorphous. Any segments that contain an end site in the amorphous region are characterized as tails. To differentiate bridges and loops, we consider the fact that bridges extend from a crystal stem through the amorphous stack and connects with a crystal stem on the other side, whereas loops enter the amorphous region but reconnects to the same crystal stack side from which they originated. By using such knowledge we can characterize the chains in the non-crystalline domain. As an example, in Figure 1 we have assembled some of the generated samples using the IMC approach and characterized their topology.

2.4. Uniaxial tensile modelling

To perform the uniaxial tensile modelling we use a deformation controlled approach, by which we apply normal strain in the normal direction of the crystalline-amorphous interface such that it concurs with the lamellar separation mode [50], see Figure 1. To ensure that the stress state retains a uniaxial character and that the temperature remains fairly constant, we utilized a barostat to apply transverse pressure corresponding to 1 atm and a thermostat to regulate the temperature to 350 K. The true strain was applied through a strain rate $\dot{\epsilon}_z = 5 \cdot 10^7$ s^{-1}, which was utilized for all tensile simulations. It should be noted that we also tried the reduced strain rate $\dot{\epsilon}_z = 2.5 \cdot 10^7$ s^{-1} for the OPLS-AA approach and found no significant differences in the resulting deformations or stress-strain curves. Even though these strain rates are high for most practical applications, it is necessary to complete the MD simulations within a reasonable time frame. Thus, lower strain rates were not investigated within the present work. The stress tensor is computed

based on the virial theorem, with the kinetic term included.

To determine a suitable timestep increment size for the simulations, the total energy drift for the all-atomic approach was studied within the NVE ensemble using different increments. This investigation revealed that for timestep increments of the size $\Delta t = 1$ fs satisfactory energy conservation could be retained, which was used for all simulations in the present work. It should be noted that a substantially larger timestep could be used for the UA approach without getting any energy drift. The explanation for this inconsistency lies in the fact that H-atoms vibrate with higher frequency than UA particles. Thus, to resolve the explicit dynamics of the H-atoms a smaller timestep is required. However, for consistency, we chose $\Delta t = 1$ fs for both the OPLS-AA and the UA simulations. Despite the simplification of neglecting Coulombic interaction in the OPLS-AA approach, it was found that the simulations in the present work using the UA approach are about 22 times faster than the explicit model.

3. Results

3.1. Topology characterization

Two sets of each ten samples were generated with either the {001} or {201} planes coinciding with the crystalline-amorphous interface. Moreover, for each set we varied the number of cut chains such that the number of bridge-molecules was varied. The computed orthorhombic lattice parameters at $T = 350$ K for the crystalline parts of the semi-crystalline setups were found to be approximately $a = 7.44$ Å, $b = 4.88$ Å and $c = 2.56$ Å in the OPLS-AA approach and $a = 7.85$ Å, $b = 4.74$ Å and $c = 2.45$ Å for the UA samples.

In Table 2, we have summarized the topology data for all the generated samples. It is seen that for both sets the number of bridge-molecules varies from none to two. Moreover, depending on how many chains are cut in the amorphous region during the IMC modelling, the relative fractions of loops and tails are very different. If we choose to cut 30 chains the tail to loop ratio is about 1.5-2, whereas for 77 cut chains the ratio becomes about 4 or higher. Thus, the topologies of the two sets of generated samples differ also in characteristics such as average chain length and entanglements, which are factors that have been reported to substantially affect the mechanical response [40, 44].

3.2. Ideal critical resolved shear stress

To investigate the potentials' predictive strengths in terms of crystal plasticity properties, we have benchmarked them against DFT modelling, as done in [14]. Such comparisons have been made possible thanks to the emergence of vdW-based exchange-correlation formulations [59, 60], which have improved the basis for DFT modelling of vdW dominated systems, such as PE [14, 24]. By evaluating the generalized stacking fault energy it has previously been shown that the OPLS-AA approach gives a better estimate of the threshold energy than the UA approach [14] (see Figure 2(a)).

By differentiating the generalized stacking fault energy curves with respect to the chain slip displacement in the [001]-direction, δ, we get the ideal critical resolved shear stress for chain slip, i.e. $\tau = d\gamma/d\delta$, as depicted in Figure 2(b). The results reveal that the shear stress maxima for DFT and OPLS-AA calculations correspond to 140 MPa and 108 MPa, respectively, whereas the UA potential gives a value of only 55 MPa, see Figure 2. The culprit behind the deviant behaviour of the UA approach is the missing explicit H-H and C-H repulsion. These interaction mechanisms are of significance for chain slip because such motion involves close-ranged passing of H-atoms of neighbouring chains. Thus, the UA approach predicts greatly underestimated critical resolved shear stress.

It is noted that the unstable stacking fault energy and the critical resolved shear stress are computed for an ideal defect-free crystal at 0 K. Consequently, the calculated critical resolved shear stress is an overestimation that cannot be directly translated to that of a practical crystal containing defects. Despite this idealization, it gives an indication of the predictability of the potentials. Compared to experimental data, which are of the order ∼10 MPa for (100)[001] chain slip [3–5, 12], the computed critical resolved shear stresses in the considered samples are substantially overestimated, which will make them more rigid than observed experimentally. This discrepancy can be partially attributed to the lattice expansion and thermal activation processes in the crystal that occur at room temperature, at which the experiments are performed. Moreover, the exaggerated resistance to slip in our computational models can be attributed to the absence of dislocations and twins that mitigate slip in the crystalline regions. Dislocations are typically present in the defect density range 10^5-10^8 cm^{-2}, which increases further during deformation to accomodate the plastic flow [4, 5]. Thus, even though thermal expansion effects are explicitly included in the modelling, the impact of crystal defects have been
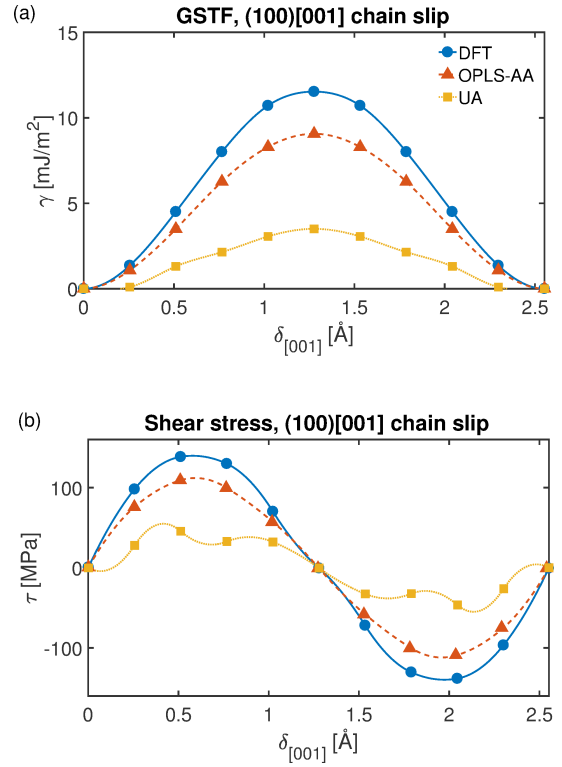

Figure 2: (a) Generalized stacking fault energy curves for (100)[001] chain slip computed using DFT, the OPLS-AA and UA approaches reproduced from [14]. (b) The corresponding ideal shear stress curve. (For interpretation of the references to colour in this figure legend, the reader is referred to the web version of this article.)

neglected in the present work but would be necessary to reduce the critical resolved shear stress to experimental levels.

3.3. Stress-strain behaviour

In Figure 3, we have summarized the stress-strain behaviour for all samples using both the OPLS-AA and UA approaches. It is seen that the stress-strain curves display a somewhat linear behaviour in the low strain region. Although the first peak stress following the linear behaviour is about 100 MPa for all simulations, the strain at which the peak occurs varies substantially. It is found to be about 6-8% for the OPLS-AA simulations and lies in the range 10-30% for the UA modelling. For the UA-modelling, it is seen that samples 1-10 (with {001} orientation) reach their peak stress at about 10-13% strain, whereas it occurs at higher strains (in the range 15-30%) for tilted samples. This is attributed to the fact that chain slip in the {201} case leads to a rotation of stems that on average accounts for about 10% strain. Beyond this strain level, the tilted configurations behave rather similarly to the {001} case, simply offset to higher strain by the amount of rotation. Thus, the computed Young's modulus is consistently lower for the tilted samples within the UA-approach. Compared to the OPLS-AA results, the calculated Young's modulus of the UA model is found to be consistently lower.

Apart from these similarities, the stress-strain behaviour of the OPLS-AA and UA models differ considerably. Most
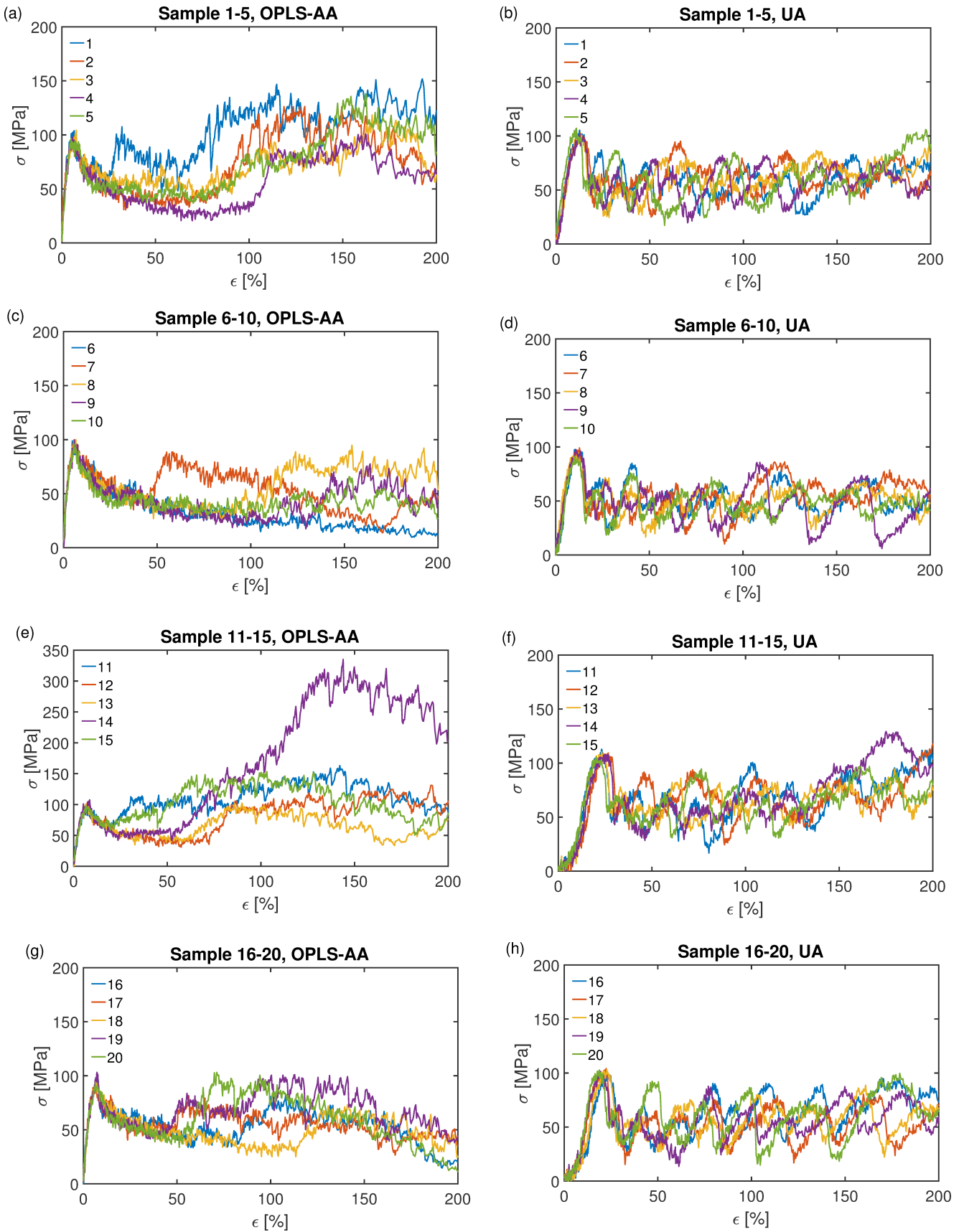
Figure 3: Uniaxial stress-strain behaviour for samples 1-20. The left column represents OPLS-AA simulations and the right column correspond to UA-based data. (For interpretation of the references to colour in this figure legend, the reader is referred to the web version of this article.)

7

notably it is seen that the UA curves oscillate substantially, whereas the all-atomic results are smoother. Such oscillating behaviour has been observed previously in references [25, 26], where it was found to be closely associated to a yielding mechanism that consists of repeated melting and chain transport from the crystalline part to the amorphous region. The same type of yielding mechanism was observed for all UA samples in the present work, regardless of the chain topology and the crystalline-amorphous interface plane.

By comparing the ultimate stresses of the OPLS-AA samples, it is seen that samples 1, 2, 4, 14 and 15 generally exhibit higher values, especially when compared with samples 6-10 and 16-20. The former of these possess fewer free chain ends and more bridge chains than the latter. Thus, as expected, increased entanglement and bridge stretching lead to increased stress levels, whereas samples with higher chain end density in the amorphous region more easily disentangle the chains, which yields reduced ultimate stress levels.

3.4. Yield analysis

To relate the stress-strain behaviour with the yielding mechanisms, we have specifically studied four samples: 1, 4, 13 and 14. They were chosen on the basis that they either display a deviant stress-strain behaviour for the OPLS-AA modelling or are deemed representative for the bulk of the samples. For these specific cases samples 4 and 13 are considered representative for the {001} and {201} samples, respectively, whereas samples 1 and 14 exhibit stresses that lie in the higher part of the spectrum.

3.4.1. {001} crystal orientation

In Figure 4 we display the configurational snapshots for samples 1 and 4 at different instances along the respective stress-strain curves for both the OPLS-AA (Figure 4(a)) and the UA (Figure 4(b)) approaches. The first observation that can be made is that the two potentials give rise to very different yielding behaviours. It is revealed that for the OPLS-AA potential we get cavity formation with highly aligned chains, which are fed from the amorphous region through the alignment of loops, bridges and tails, see Figure 4(a). Interestingly, virtually no lateral contraction is observed. These features correspond to those of the lamellar separation mechanism [4, 50], which is expected since the normal loading direction coincides with the crystal-amorphous interface normal. For the OPLS-AA modelling, it is noted that sample 1 exhibits a generally higher stress amplitude than sample 4. This is related to the fact that two cavities are formed for sample 1, as opposed one cavity for sample 4, as seen in Figure 4(a).

Repetitive melting and chain transport from the crystalline region to the amorphous domain is observed for the UA approach, in accordance with [25, 26], see Figure 4(b). This mechanism was observed for all UA simulations regardless of topology. It is further found that the UA-samples undergo substantial contraction in the transverse directions, indicating a significant Poisson effect. Inspection of the initial configurations of the crystalline parts of the UA samples reveal that the stems

are slightly tilted relative to the vertical direction. Such response is particularly noticeable in the top sequence of Figure 4(b), which implies that the interface plane is slightly perturbed from {001} to {κ, 0, 1}, where κ is a relatively small value. However, as the tensile strain is applied, the chains in the crystals align in the tensile direction even at small strains, see Figure 4(b). This is an indication that the UA crystal undergoes crystal reorientation/fine chain slip already at small strains. Such behaviour is not observed for the OPLS-AA approach. In fact, no notable chain slip was found to occur at any strain for the {001}-samples in the explicit modelling. Another related observation is the fact that the interface between the amorphous and crystalline parts remains planar during the tensile simulations for the all-atomic approach. Such lack of plasticity in the crystalline parts is believed to be related to the fact that the Schmid factor is zero when the chains are aligned in the tensile direction. This would imply that the stresses appearing locally in the crystalline-amorphous interface as a consequence of stretched loops, tails and bridge-molecules are not sufficient to trigger chain slip. The opposite behaviour is seen for the UA simulations. Despite that the interfaces seem to be approximately planar initially - relatively early on there is chain slip occurring that causes the interface to become wavy or wedge like. Such events were found to occur even at low strains, < 20%, see Figure 4(b). Thus, cavity formation is dominant and the occurrence of chain slip is very limited in the OPLS-AA frame, whereas in the UA approach chain slip is frequently occurring, even at early stages of the deformation. These results indicate a substantial discrepancy between the modelling approaches, which is related to the disparately predicted critical resolved shear stress of the models.

3.4.2. {201} crystal orientation

In Figure 5 we have performed the same type of evaluation for samples 13 and 14, which both have the {201} crystal orientation. The OPLS-AA stress-strain curves reveal that there is a drastic increase in stress for sample 14 at about 100% strain, at which the stress is approximately doubled from 150 MPa to 300 MPa. Inspection of atomic configurations reveal that this increase is related to crystal reorientation, which occurs when the chains start to align in the tensile direction, see Figure 5(a). To investigate this closer we studied how the tilt angle, Θ, varies with strain for the tilted samples 11-20, see Figure 6. It is a measure of the misalignment between the crystal chains and the tensile direction. It is seen that it initially corresponds to about 34° for all samples, which is in agreement with the ideal tilt angle value for samples with the crystalline-amorphous interface corresponding to the {201} plane. As the strain increases, for sample 13 the tilt angle remains virtually unchanged, see Figure 6(a). However, for samples 11-12 and 14-15 it gradually decreases above $\epsilon \approx 100\%$. This suggests that the crystal eventually reorients through chain slip such that the chains align with the tensile direction and the crystalline-amorphous interface plane becomes slightly wavy. The point at which deviation from $\Theta \approx 34°$ starts and the amount of reorientation observed varies for the different samples, but the onset of cavity formation precedes crystalline yielding substantially, as seen
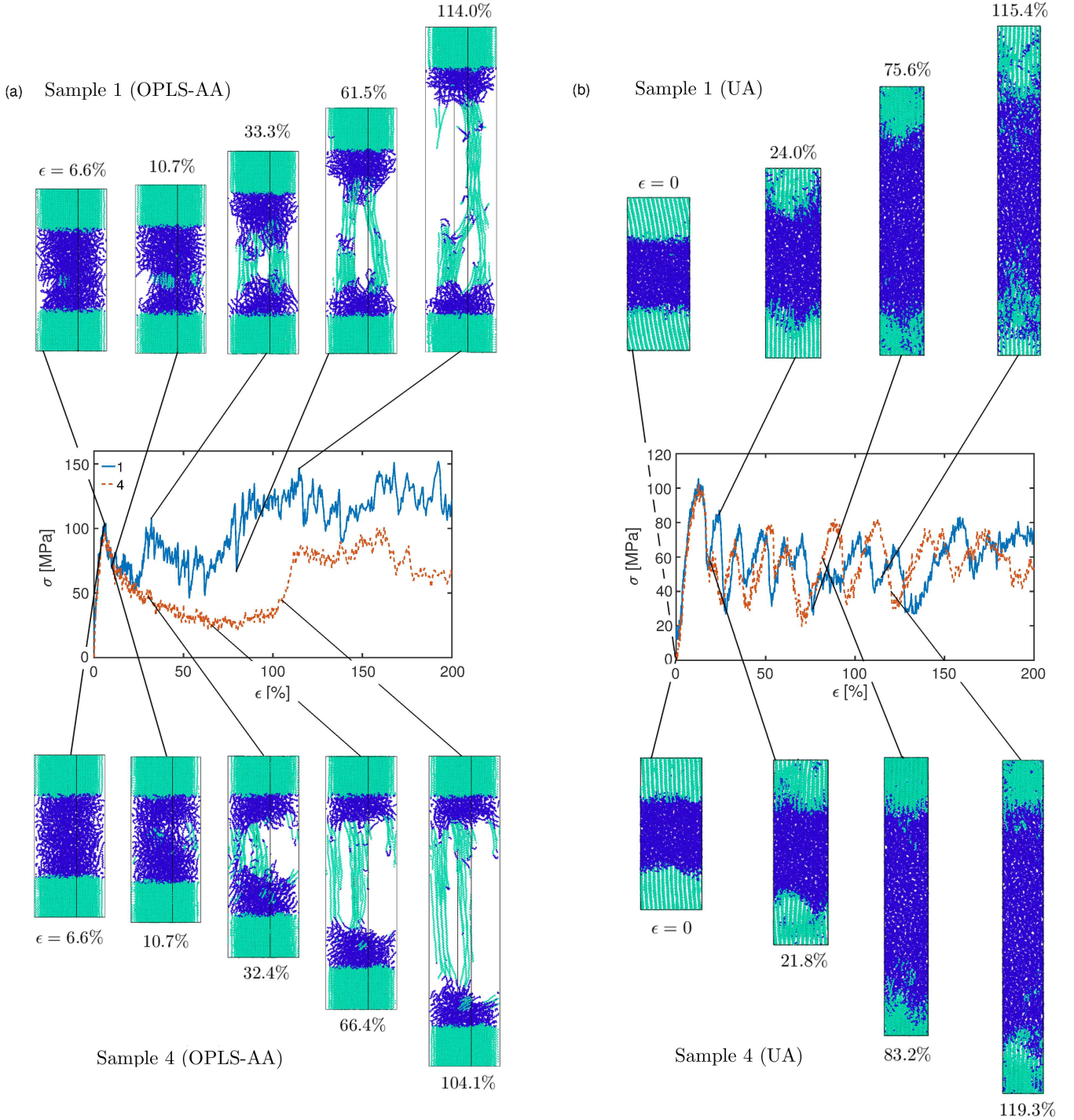
Figure 4: Yielding behaviour for samples 1 and 4 using (a) the OPLS-AA and (b) the UA force-fields. The top sequences correspond to sample 1 and the bottom are those of sample 4. For the OPLS-AA approach all H-atoms have been filtered out. The springgreen sites are designated to be crystalline and blue atoms amorphous based on the computed value of Herman's orientation parameter. (For interpretation of the references to colour in this figure legend, the reader is referred to the web version of this article.)

in Figure 5(a).

The upper limit normal stress (estimated using data computed at $T = 0$ K) for which we should get chain slip for the tilted {201} systems can be approximated by the Schmid factor as $\sigma = \tau_{CRSS}/(\cos\chi\cos\lambda)$ [4] where τ_{CRSS} is the ideal critical resolved shear stress, $\chi = 56°$ and $\lambda = 34°$ for the initial tilt.

They correspond to 232 MPa and 118 MPa for the OPLS-AA and UA approaches, respectively. For the OPLS-AA potential, the most notable crystal reorientation was observed for sample 14 and, as can be seen in Figure 3 and 5, it is associated with high stresses that exceed the ideal value. Although the averaged peak normal stresses of samples 11-12 and 15 do not exceed the
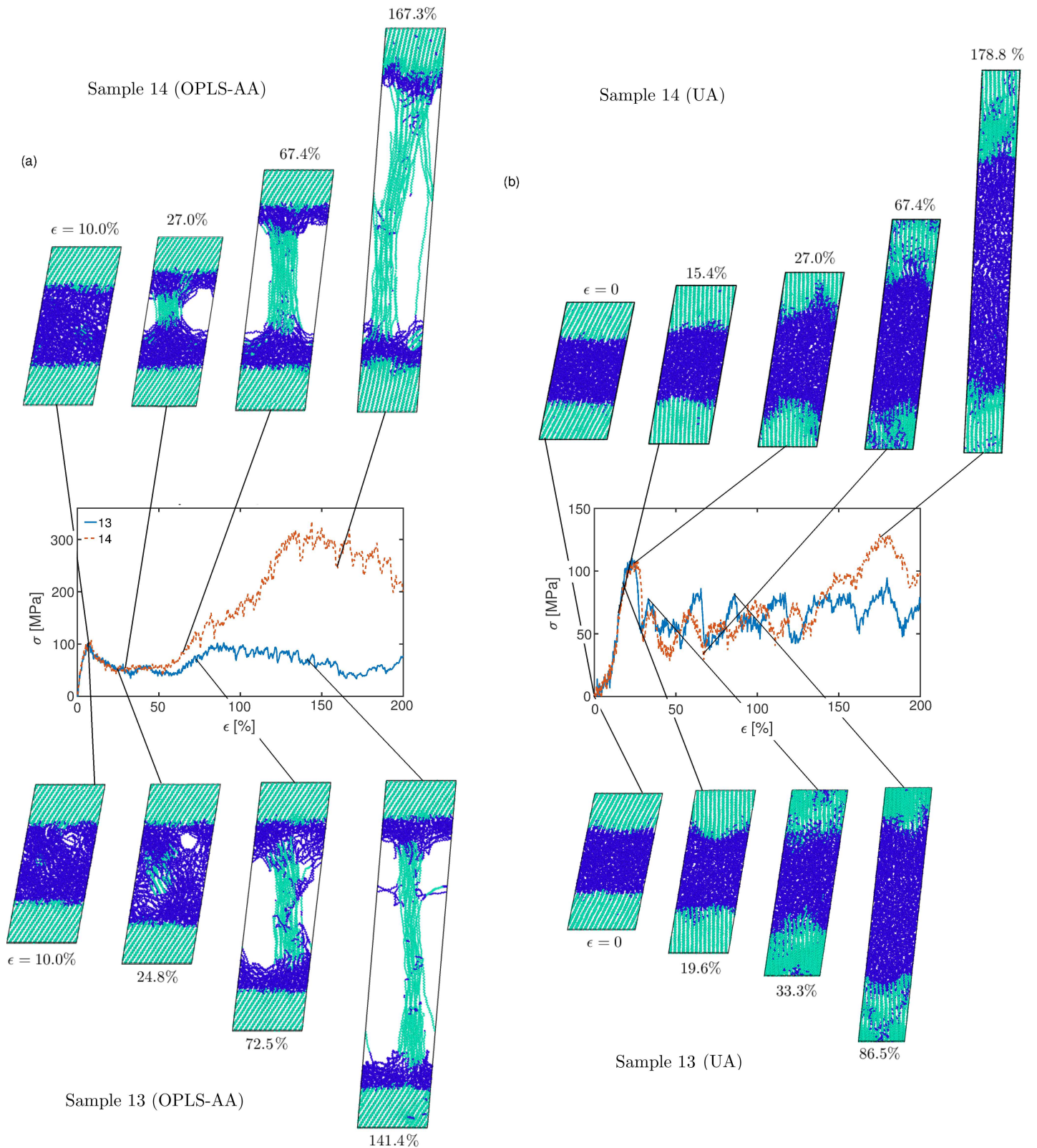
Figure 5: Yielding behaviour for samples 13 and 14 using (a) the OPLS-AA and (b) the UA force-fields. The top sequences correspond to sample 14 and the bottom are those of sample 13. For the OPLS-AA approach all H-atoms have been filtered out. The springgreen sites are designated to be crystalline and blue atoms amorphous based on the computed value of Herman's orientation parameter. (For interpretation of the references to colour in this figure legend, the reader is referred to the web version of this article.)
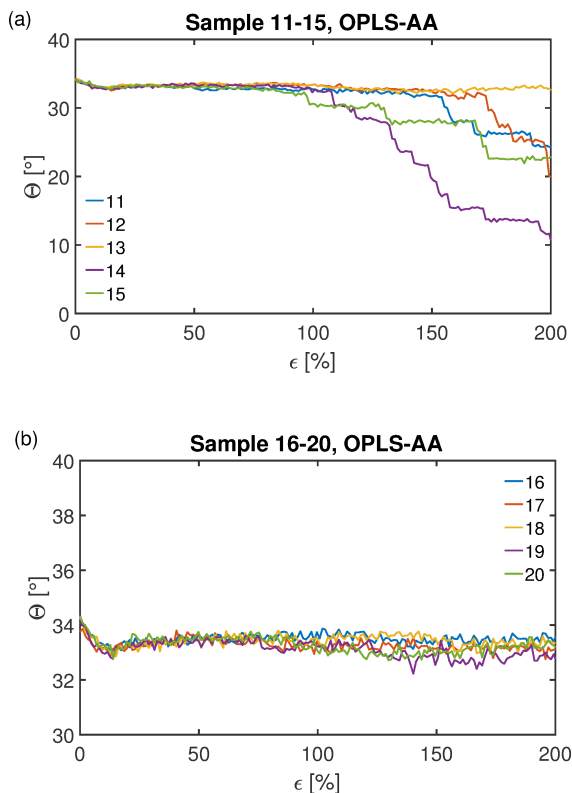
Figure 6: Illustration of crystal stem orientation vs. strain for (a) samples 11-15 and (b) samples 16-20. The tilt angle, Θ, is defined as the angle between the strain direction and the averaged chain direction in the crystalline part. (For interpretation of the references to colour in this figure legend, the reader is referred to the web version of this article.)

computed barrier value, they most likely do that locally at the crystal-amorphous interface that gives rise to the observed limited chain slip for those samples.

For samples 16-20 no chain reorientation was observed, see Figure 6(b). These samples have fewer bridge molecules and loops and a larger number of tail sites than samples 11-15, which affect the applied resolved shear stress in the lamellae and, consequently, the onset of chain slip. These model predictions imply that there is substantial resistance to chain slip, and it is preferential for the amorphous phase first to undergo plastic deformations rather than the crystals. Yet, depending on the topological characteristics specific to the sample, chain slip may occur at later stages if the shear stresses locally in the slip planes of the crystal are high enough.

For the UA force-field the yielding behaviour differs substantially from that of the OPLS-AA. Although initially tilted, for all simulations the crystal chains align in the tensile direction already during the initial stress ramp up that occurs before the first peak stress is reached. This occurs at about $\epsilon \approx 20\%$ and approximately coincides with the normal stresses reaching the upper limit normal stress required for chain slip, i.e. $\sigma \approx 118$ MPa (see Figure 5(b)). Likewise to the {001} systems, we also observe significant chain slip for the {201} crystal orientation, which leads to a wavy crystalline-amorphous interface. Thus, as previously noted, the chain slip for the UA approach occurs

at a lower strain than the all-atomic approach.

As a side note, it is observed that there is a substantial peak stress at about 180% strain for sample 14, see Figure 5(b). This stress-strain curve behaviour is reminiscent of that observed for the OPLS-AA approach, at which the crystals start to initiate the reorientation. However, as can be seen by the top insets in Figure 5(b), no chain reorientation occurs at that point and the high stress amplitude is merely a part of the oscillating behaviour and the deformation follows the aforementioned repeated melting mechanism.

4. Discussion

In the present section, we discuss the considered potentials' impact on the results and address the implications of the adopted idealized modelling setup compared to experimental results of real PE semi-crystals.

In light of the fact that both herein utilized potentials are empirical, the transferability and predictability of them both are limited. They represent two different levels of coarse-graining. Seen from the electronic scale, the different bonding components are replaced by effective potentials of relatively simple parametric types to reduce the computational effort. The OPLS-AA approach retains a full explicit model, whereas the coarse-graining is driven further in the UA approach such that the repeat units are lumped together as super atoms with the intramolecular interaction described by a L-J potential. The consequences of this reduction of degrees of freedom and the simplified interaction model are that the interaction between repeat units of neighbouring chains becomes spherical and that explicit close-ranged interaction between H-atoms and C-H atoms are only represented in some averaged sense. For the case of chain slip, typically chains are translated relative to each other in the [001]-direction such that H-atoms of neighbouring chains pass each other at very close distance. This would suggest that the explicit H-H interaction is required to represent the resistance to such motion. Thus, it can be argued that the UA approach does not provide sufficient resolution to quantitatively capture the energy barriers and internal friction responsible for the most dominant yielding mechanism in the crystalline region.

For modelling lamellar separation, the low energy barriers of the UA approach manifest in a yielding mechanism of repeated melting and chain transport from the crystalline part to the amorphous region. This is in contrast to cavity formation, which is seen in the all-atomic modelling and is closely associated with the lamellar separation mode [50]. Similar types of inconsistencies have been observed when modelling rheological properties in liquid polymers, see for instance [61–64], and it implies that time-scaling is necessary to associate the observed mechanisms with experimental or all-atomic results. This behaviour suggests that the potentials have intrinsic rates or activation times for competing mechanisms, which is in line with previously reported results that have demonstrated a clear strain rate dependence [26]. The outcomes from that work clearly shows that the yielding mechanisms can change from cavitation formation to repeated melting when the strain rate is reduced by

an order of magnitude. This implies that the competition of the mechanisms and the observed behaviour are dictated by the intrinsic rates and the applied strain rate.

Since UA-potentials typically exhibit generally low chain slip energy barriers, the rate associated with such yielding is likely faster than for explicit models. It is because of this discrepancy and the fact that UA models are typically fitted to reproduce equilibrium properties [45], that the observed yielding mechanisms vary significantly when performing non-equilibrium high-strain rate MD simulations, such as in the present work. We do, however, anticipate that the intrinsic UA rates could be slowed down by utilizing a dissipative particle dynamics thermostat [65], which would partially inhibit the chain slip in the UA model and promote a more similar response to that of the explicit model.

The modelling setups of the present work rely on a few idealizations that need to be addressed to understand their limitations. Because of the high applied strain rate ($\dot{\epsilon}_z = 5 \cdot 10^7$ s^{-1}) and the high energy barriers associated with chain slip for the explicit model, we expect that the results are not directly transferable to experimental observations. This is because the intrinsic rates of the mechanisms associated with visco-plastic yielding of explicit models are too slow to be resolved within a reasonable time frame of an explicit MD simulation. Moreover, we have considered a semi-crystalline lamellar stack geometry, in which the crystalline regions are free of dislocations. Such defects contribute to the reduction of energy and shear stress barriers for chain slip compared to those for idealized defect-free crystals [3, 5, 12]. These idealizations inhibit chain slip for the {201} tilted OPLS-AA samples, as seen in the results.

In light of these limitations, it can be argued that it instead would be suitable to utilize a UA force-field to account for the presence of crystal defects in a mean-field sense without explicitly introducing them in the atomistic model. However, much care would have to be practised when setting up such a model and interpreting the results, mainly for three reasons: (i) it is likely that the disturbances emanating from discrete dislocations may induce high local stresses that cannot be accurately captured in a mean-field manner, (ii) careful time re-scaling must be made to associate the passage of events with those of an experimental PE sample and (iii) transferability would likely be limited.

5. Summary and conclusions

In the present work we have performed a comparative classical atomistic study of the stress-strain and yielding behaviours of semi-crystalline lamellar PE by using all-atomic OPLS and coarse-grained UA force-fields. We consider two sets of semi-crystalline samples where the crystalline-amorphous interfaces correspond to either {001} or {201} planes, that are perpendicular to the loading direction such that the loading conditions resemble those of the lamellar separation mode.

The results show that depending on the utilized interatomic potential, the stress-strain and yielding behaviours vary significantly. Compared to the conjectured behaviour of lamellar separation, the all-atomic model reproduces the main yielding

characteristics of such loading conditions. This means primarily cavity formation with no or limited lateral contraction, accompanied by no or limited plastic deformations in the crystal, depending on if the chains are initially aligned or tilted relative to the tensile direction.

The results obtained when using the UA approach are very different from those of the explicit model. It is predicted that yielding occurs by repeated melting and chain transport into the amorphous domain. These results show that the average nature of this coarse-grained approach lowers activation energy barriers to such an extent that the overall deformation behaviour and yielding mechanisms change substantially.

The discrepancies of the models can be attributed to that yielding of the crystalline region is very limited when explicit H-H and C-H repulsion is present. Such interaction inhibits chain slip by increasing the critical resolved shear stress of the crystal. Thus, in the case of the coarse-grained UA approach, for which the force components in question are missing, the critical resolved shear stress becomes severely underestimated. This leads to substantial amounts of chain slip and crystal re-orientation. The disparate energy and shear stress barriers for chain slip observed for the different models can be interpreted as different intrinsic activation rates for the observed yielding mechanisms. This implies that the competition between mechanisms is strain rate dependent, which ultimately gives rise to different responses for the two modelling approaches.

References

[1] S. S. Katti, M. Schultz, The microstructure of injection-molded semicrystalline polymers: A review, Polym. Engng. Sci. 22 (16) (1982) 1001–1017.

[2] R. Young, P. Lovell, Introduction to Polymers, Third Edition, Taylor & Francis, 2011.

[3] L. Lin, A. S. Argon, Structure and plastic deformation of polyethylene, J. Mater. Sci. 29 (2) (1994) 294–323.

[4] Z. Bartczak, A. Galeski, Plasticity of semicrystalline polymers, Macromol. Symp. 294 (1) (2010) 67–90.

[5] A. Galeski, Strength and toughness of crystalline polymer systems, Prog. Polym. Sci. 28 (12) (2003) 1643 – 1699.

[6] A. S. Argon, The Physics of Deformation and Fracture of Polymers, Cambridge University Press, 2013.

[7] P. B. Bowden, R. J. Young, Deformation mechanisms in crystalline polymers, J. Mater. Sci. 9 (12) (1974) 2034–2051.

[8] A. Rozanski, A. Galeski, Plastic yielding of semicrystalline polymers affected by amorphous phase, Int. J. Plast. 41 (2013) 14 – 29.

[9] M. Uchida, N. Tada, Micro-, meso- to macroscopic modeling of deformation behavior of semi-crystalline polymer, Int. J. Plast. 49 (2013) 164 – 184.

[10] J. Petermann, H. Gleiter, Direct observation of dislocations in polyethylene crystals, Philos. Mag. 25 (4) (1972) 813–816.

[11] A. Cowking, J. G. Rider, On molecular and textural reorientations in polyethylene caused by applied stress, J. Mater. Sci. 4 (12) (1969) 1051–1058.

[12] R. J. Young, P. B. Bowden, J. M. Ritchie, J. G. Rider, Deformation mechanisms in oriented high-density polyethylene, J. Mater. Sci. 8 (1) (1973) 23–36.

[13] A. Galeski, Z. Bartczak, A. S. Argon, R. E. Cohen, Morphological alterations during texture-producing plastic plane strain compression of high-density polyethylene, Macromol. 25 (21) (1992) 5705–5718.

[14] P. A. T. Olsson, E. Schröder, P. Hyldgaard, M. Kroon, E. Andreasson, E. Bergvall, Ab initio and classical atomistic modelling of structure and defects in crystalline orthorhombic polyethylene: Twin boundaries, slip interfaces, and nature of barriers, Polymer 121 (2017) 234 – 246.

[15] H. Gleiter, A. S. Argon, Plastic deformation of polyethylene crystals, Philos. Mag. 24 (187) (1971) 71–80.

[16] V. F. Holland, Dislocations in polyethylene single crystals, J. Appl. Phys. 35 (11) (1964) 3235–3241.

[17] P. Allan, M. Bevis, Deformation processes in thin melt-cast films of high-density polyethylene: II. Deformation processes in the non-equatorial regions of spherulites, Philos. Mag. A 41 (4) (1980) 555–572.

[18] F. C. Frank, A. Keller, A. O'Connor, H. H. Wills, Deformation processes in polyethylene interpreted in terms of crystal plasticity, Philos. Mag. 3 (25) (1958) 64–74.

[19] R. J. Young, P. B. Bowden, Twinning and martensitic transformations in oriented high-density polyethylene, Philos. Mag. 29 (5) (1974) 1061–1073.

[20] P. Allan, M. Bevis, Deformation processes in thin melt-cast films of high-density polyethylene: I. Experimental methods and deformation processes in the equatorial regions of spherulites, Philos. Mag 35 (2) (1977) 405–430.

[21] M. Bevis, E. Crellin, The geometry of twinning and phase transformations in crystalline polyethylene, Polymer 12 (11) (1971) 666 – 684.

[22] P. Allan, E. B. Crellin, M. Bevis, Stress-induced twinning and phase transformations in polyethylene single crystals, Philos. Mag. 27 (1) (1973) 127–145.

[23] P. Allan, M. Bevis, Multiple deformation processes in polyethylene single crystals, Philos. Mag. 31 (5) (1975) 1001–1009.

[24] P. A. T. Olsson, P. Hyldgaard, E. Schröder, E. Persson Jutemar, E. Andreasson, M. Kroon, Ab initio investigation of monoclinic phase stability and martensitic transformation in crystalline polyethylene, Phys. Rev. Materials 2 (2018) 075602.

[25] I.-C. Yeh, J. L. Lenhart, G. C. Rutledge, J. W. Andzelm, Molecular dynamics simulation of the effects of layer thickness and chain tilt on tensile deformation mechanisms of semicrystalline polyethylene, Macromol. 50 (4) (2017) 1700–1712.

[26] I.-C. Yeh, J. W. Andzelm, G. C. Rutledge, Mechanical and structural characterization of semicrystalline polyethylene under tensile deformation by molecular dynamics simulations, Macromol. 48 (12) (2015) 4228–4239.

[27] J. M. Kim, R. Locker, G. C. Rutledge, Plastic deformation of semicrystalline polyethylene under extension, compression, and shear using molecular dynamics simulation, Macromol. 47 (7) (2014) 2515–2528.

[28] S. Lee, G. C. Rutledge, Plastic deformation of semicrystalline polyethylene by molecular simulation, Macromol. 44 (8) (2011) 3096–3108.

[29] A. Ghazavizadeh, G. C. Rutledge, A. A. Atai, S. Ahzi, Y. Remond, N. Soltani, Micromechanical characterization of the interphase layer in semi-crystalline polyethylene, J. Polymer Sci. B: Polymer Phys. 51 (16) (2013) 1228–1243.

[30] P. J. in 't Veld, M. Hütter, G. C. Rutledge, Temperature-dependent thermal and elastic properties of the interlamellar phase of semicrystalline polyethylene by molecular simulation, Macromol. 39 (1) (2006) 439–447.

[31] N. Lempesis, P. J. in 't Veld, G. C. Rutledge, Atomistic simulation of a thermoplastic polyurethane and micromechanical modeling, Macromol. 50 (18) (2017) 7399–7409.

[32] S. Zhu, N. Lempesis, P. J. in 't Veld, G. C. Rutledge, Molecular simulation of thermoplastic polyurethanes under large tensile deformation, Macromol. 51 (5) (2018) 1850–1864.

[33] N. Lempesis, P. J. in 't Veld, G. C. Rutledge, Atomistic simulation of the structure and mechanics of a semicrystalline polyether, Macromol. 49 (15) (2016) 5714–5726.

[34] S. Pandiyan, B. Rousseau, Factors influencing properties of interfacial regions in semicrystalline polyethylene: A molecular dynamics simulation study, Polymer 54 (14) (2013) 3586 – 3593.

[35] L. Ding, R. L. Davidchack, J. Pan, A molecular dynamics study of Young's modulus change of semi-crystalline polymers during degradation by chain scissions, J. Mech. Behav. Biomed. 5 (1) (2012) 224 – 230.

[36] V. Kumar, C. R. Locker, P. J. in 't Veld, G. C. Rutledge, Effect of short chain branching on the interlamellar structure of semicrystalline polyethylene, Macromol. 50 (3) (2017) 1206–1214.

[37] A. L. Brayton, I.-C. Yeh, J. W. Andzelm, G. C. Rutledge, Vibrational analysis of semicrystalline polyethylene using molecular dynamics simulation, Macromol. 50 (17) (2017) 6690–6701.

[38] X. Dong, D. L. McDowell, S. R. Kalidindi, K. I. Jacob, Dependence of mechanical properties on crystal orientation of semi-crystalline polyethylene structures, Polymer 55 (16) (2014) 4248 – 4257.

[39] B. Monasse, S. Queyroy, O. Lhost, Molecular dynamics prediction of elastic and plastic deformation of semi-crystalline polyethylene, Int. J. Mater. Form. 1 (1) (2008) 1111–1114.

[40] S. Queyroy, B. Monasse, Effect of the molecular structure of semicrystalline polyethylene on mechanical properties studied by molecular dynamics, J. Appl. Polym. Sci. 125 (6) (2012) 4358–4367.

[41] F. Nilsson, X. Lan, T. Gkourmpis, M. Hedenqvist, U. Gedde, Modelling tie chains and trapped entanglements in polyethylene, Polymer 53 (16) (2012) 3594 – 3601.

[42] A. Moyassari, H. Mostafavi, T. Gkourmpis, M. Hedenqvist, U. Gedde, F. Nilsson, Simulation of semi-crystalline polyethylene: Effect of short-chain branching on tie chains and trapped entanglements, Polymer 72 (2015) 177 – 184.

[43] S. Jabbari-Farouji, J. Rottler, O. Lame, A. Makke, M. Perez, J.-L. Barrat, Plastic deformation mechanisms of semicrystalline and amorphous polymers, ACS Macro Lett. 4 (2) (2015) 147–150.

[44] S. Jabbari-Farouji, O. Lame, M. Perez, J. Rottler, J.-L. Barrat, Role of the intercrystalline tie chains network in the mechanical response of semicrystalline polymers, Phys. Rev. Lett. 118 (2017) 217802.

[45] F. Müller-Plathe, Coarse-graining in polymer simulation: From the atomistic to the mesoscopic scale and back, Chem. Phys. Chem. 3 (9) (2002) 754–769.

[46] A. Pawlak, Cavitation during tensile deformation of high-density polyethylene, Polymer 48 (5) (2007) 1397 – 1409.

[47] A. Pawlak, A. Galeski, Cavitation during tensile drawing of annealed high density polyethylene, Polymer 51 (24) (2010) 5771 – 5779.

[48] A. Pawlak, A. Galeski, A. Rozanski, Cavitation during deformation of semicrystalline polymers, Prog. Poly. Sci. 39 (5) (2014) 921 – 958.

[49] V. Vitek, Intrinsic stacking faults in body-centred cubic crystals, Philos. Mag. 18 (154) (1968) 773–786.

[50] A. Keller, D. P. Pope, Identification of structural processes in deformation of oriented polyethylene, J. Mater. Sci. 6 (6) (1971) 453–478.

[51] S. Plimpton, Fast parallel algorithms for short-range molecular dynamics, J. Comput. Phys. 117 (1) (1995) 1 – 19.
URL http://lammps.sandia.gov

[52] G. Shrivastav, M. Agarwal, Stress-strain relationships in hydroxyl substituted polyethylene, J. Phys. Chem. B 120 (30) (2016) 7598–7605.

[53] W. L. Jorgensen, D. S. Maxwell, J. Tirado-Rives, Development and testing of the OPLS all-atom force field on conformational energetics and properties of organic liquids, J. American Chem. Soc. 118 (45) (1996) 11225–11236.

[54] W. L. Jorgensen, J. Tirado-Rives, The OPLS [optimized potentials for liquid simulations] potential functions for proteins, energy minimizations for crystals of cyclic peptides and crambin, J. American Chem. Soc. 110 (6) (1988) 1657–1666.

[55] W. Paul, D. Y. Yoon, G. D. Smith, An optimized united atom model for simulations of polymethylene melts, J. Chem. Phys. 103 (4) (1995) 1702–1709.

[56] K. Bolton, S. B. M. Bosio, W. L. Hase, W. F. Schneider, K. C. Hass, Comparison of explicit and united atom models for alkane chains physisorbed on α-Al$_2$O$_3$ (0001), J. Phys. Chem. B 103 (19) (1999) 3885–3895.

[57] P. J. in 't Veld, G. C. Rutledge, Temperature-dependent elasticity of a semicrystalline interphase composed of freely rotating chains, Macromol. 36 (19) (2003) 7358–7365.
URL http://montecarlo.sourceforge.net/emc/Welcome.html

[58] A. Stukowski, Visualization and analysis of atomistic simulation data with ovito - the open visualization tool, Modelling and Simulation in Materials Science and Engineering 18 (1) (2010) 015012.

13

URL http://ovito.org/

[59] K. Berland, C. A. Arter, V. R. Cooper, K. Lee, B. I. Lundqvist, E. Schröder, T. Thonhauser, P. Hyldgaard, van der Waals density functionals built upon the electron-gas tradition: Facing the challenge of competing interactions, J. Chem. Phys. 140 (18) (2014) 18A539.

[60] K. Berland, P. Hyldgaard, Exchange functional that tests the robustness of the plasmon description of the van der Waals density functional, Phys. Rev. B 89 (2014) 035412.

[61] V. A. Harmandaris, Quantitative study of equilibrium and non-equilibrium polymer dynamics through systematic hierarchical coarse-graining simulations, Korea. Aust. Rheol. J. 26 (1) (2014) 15–28.

[62] P. Depa, C. Chen, J. K. Maranas, Why are coarse-grained force fields too fast? a look at dynamics of four coarse-grained polymers, J. Chem. Phys. 134 (1) (2011) 014903.

[63] H. A. Karimi-Varzaneh, N. F. A. van der Vegt, F. Müller-Plathe, P. Carbone, How good are coarse-grained polymer models? a comparison for atactic polystyrene, Chem. Phys. Chem. 13 (15) (2012) 3428–3439.

[64] J. Ramos, J. Vega, J. Martinez-Salazar, Predicting experimental results for polyethylene by computer simulation, Eur. Poly. J. 99 (2018) 298 – 331.

[65] P. Espanol, P. Warren, Statistical mechanics of dissipative particle dynamics, Europhys. Lett. 30 (4) (1995) 191.